



---

# State estimation of convective storms with a two-moment microphysics scheme and an ensemble Kalman filter: Experiments with simulated radar data

Ming Xue,<sup>a,b\*</sup> Youngsun Jung<sup>a,b</sup> and Guifu Zhang<sup>a</sup>

<sup>a</sup>*School of Meteorology, University of Oklahoma, Norman, Oklahoma, USA*

<sup>b</sup>*Center for Analysis and Prediction of Storms, University of Oklahoma, Norman, Oklahoma, USA*

\*Correspondence to: Ming Xue, Center for Analysis and Prediction of Storms, National Weather Center, Suite 2500, 120 David L. Boren Blvd, Norman, Oklahoma 73072, USA. E-mail: mxue@ou.edu

---

The ability of the ensemble Kalman filter method to estimate an increased number of state variables associated with a double-moment (DM) microphysics scheme is examined for the first time through observing system simulation experiments, assuming either a perfect or imperfect prediction model and/or observation operators. With the DM scheme, mixing ratios and total number concentrations of hydrometeor species are predicted.

It is found that the increased number of state variables can be reasonably well estimated when both radial velocity ( $V_r$ ) and reflectivity ( $Z_H$ ) observations are used and when the prediction model is assumed to be perfect. However, the errors increase significantly when  $Z_H$  is used alone. In this case, the filter has difficulty in estimating independently-varying mixing ratios and number concentrations, which are both directly involved in the calculation of  $Z_H$ . The addition of  $V_r$  data helps alleviate a problem associated with the solution not being sufficiently constrained by observations.

With the DM scheme, the correlations between  $Z_H$  and model state variables exhibit complex spatial structures that depend on the location of the  $Z_H$  observation. Collocated  $Z_H$  and vertical velocity show negative correlation when the observation is taken where ice phase hydrometeors are dominant, but positive correlation when it is taken where large quantities of liquid hydrometeors exist. Further study is needed to fully understand the complex correlation structures.

Imperfect model experiments were performed, with two types of model errors: (1) microphysical parametrization error due to incorrectly assumed shape parameter of the gamma particle size distribution (PSD), and (2) different ways of calculating hydrometeor scattering. The results show that the model error degrades the state estimation in general. Nevertheless, the estimated states are still reasonably good when both  $V_r$  and  $Z_H$  are assimilated. Perturbing the shape parameter of gamma PSDs within the forecast ensemble improves the overall state estimation. Copyright © 2010 Royal Meteorological Society

*Key Words:* two-moment microphysics scheme; ensemble Kalman filter; EnKF; data assimilation; model error; convective storm

*Received 2 October 2009; Revised 18 December 2009; Accepted 13 January 2010; Published online in Wiley InterScience 22 March 2010*

*Citation:* Xue M, Jung Y, Zhang G. 2010. State estimation of convective storms with a two-moment microphysics scheme and an ensemble Kalman filter: Experiments with simulated radar data. *Q. J. R. Meteorol. Soc.* **136**: 685–700. DOI:10.1002/qj.593

## 1. Introduction

Numerical weather prediction (NWP) is an initial and boundary value problem: the accuracy of the model solution depends on the accuracy of the initial condition, given appropriate boundary conditions. Therefore, extensive efforts have been devoted to developing advanced data assimilation methods that seek to minimize errors in the initial condition (e.g. Le Dimet and Talagrand, 1986; Courtier and Talagrand, 1987; Talagrand and Courtier, 1987; Evensen, 1994; Houtekamer and Mitchell, 1998; Whitaker and Hamill, 2002).

Several past studies have shown that the ensemble Kalman filter (EnKF) techniques can be successfully applied to the convective scale through both Observing System Simulation Experiments (OSSEs) and real-data experiments (e.g. Snyder and Zhang, 2003; Dowell *et al.*, 2004; Tong and Xue, 2005, hereafter TX05; Xue *et al.*, 2006, hereafter XTD06). With OSSEs, realistic observations are simulated, usually from model output, and assimilated back into the model to test data assimilation capabilities and study data impact (Lord *et al.*, 1997). The fact that the EnKF technique is capable of handling complex and highly nonlinear processes involved in the data assimilation (DA) makes it attractive for convective-scale applications, where nonlinearity tends to be strong.

However, the model forecast can also be hampered by model errors that can arise from many sources, including those due to insufficient spatial and/or temporal resolution, and misrepresentation of the physical and subgrid-scale processes. It is suggested that the model error can dominate the error growth in NWP forecasts, even if they start from rather accurate initial conditions (Zhu and Navon, 1999; Houtekamer *et al.*, 2005). Therefore, reducing the prediction model error is equally important.

The structure and time evolution of model-simulated convective storms have been found to be highly sensitive to the particle size distributions (PSDs) of the hydrometeors involved in the microphysics parametrization schemes (McCumber *et al.*, 1991; Ferrier *et al.*, 1995; Gilmore *et al.*, 2004; van den Heever and Cotton, 2004; Tong and Xue, 2008a). Different microphysical species interact with each other through complex microphysical processes including condensation/deposition, collision and coalescence, break-up, freezing/melting, evaporation/sublimation, and precipitation sedimentation. The commonly used bulk microphysics parametrization (BMP) schemes (or simply 'scheme') try to model the integrated effects of such microphysical processes involving species having their own PSDs. As a result, PSD-related parameters explicitly appear in the equations of most microphysical processes and influence the magnitude and relative importance of those processes. For example, many small raindrops in the downdraught area will evaporate faster than fewer larger drops, hence inducing a stronger cold pool which can alter the dynamic behaviour of model thunderstorms (Snook and Xue, 2008). Therefore, accurate modelling of microphysical PSDs can have a profound impact on simulated/predicted precipitating systems.

The so-called gamma distribution is often used to model the PSDs of microphysical species. With this distribution, the equation for the number concentration is

$$N_x(D) = N_{0x} D^{\alpha_x} e^{-\lambda_x D}, \quad (1)$$

where  $N(D)$  is the number density as a function of particle diameter  $D$ ,  $N_0$  is the intercept parameter,  $\lambda$  the slope parameter and  $\alpha$  the shape parameter of the PSD. Subscript  $x$  refers to one of the species. When  $\alpha_x = 0$ , (1) reduces to the commonly used exponential PSD

$$N_x(D) = N_{0x} \exp(-\lambda_x D), \quad (2)$$

that was introduced by Marshall and Palmer (1948). Ulbrich (1983) suggested that the gamma distribution better characterizes many observed raindrop size distributions, and indeed the additional free parameter allows for more flexibility in describing the relative number concentrations of large vs. small drops in a given distribution.

The  $p^{\text{th}}$  moment of this PSD is given by:

$$M_x(p) = \frac{N_{Tx} \Gamma(1 + \alpha_x + p)}{\lambda_x^p \Gamma(1 + \alpha_x)}. \quad (3)$$

The zeroth moment of the PSD is equal to the total number concentration, while the third and sixth moments of the PSD are proportional to the mass (mixing ratio) and radar reflectivity factor, respectively. For gamma distribution, when three moments are known (e.g. predicted), all three free parameters of the PSD are uniquely determined. This is the basis of multi-moment (MM) BMP schemes.

Single-moment (SM) BMP schemes, such as the commonly used Lin *et al.* (1983) and Hong and Lim (2006) schemes, usually assume an exponential PSD with specified intercept parameters for most species. Such schemes predict mixing ratios that are proportional to the third moment. SM schemes are widely used in research and operational NWP models because of their relatively low computational cost. When the intercept parameters of the PSDs are specified, the scheme does not allow for independent variations in the shape or intercept parameters that can result from differential conversion, differential sedimentation, shear motion of the atmosphere or other processes. Kumjian and Ryzhkov (2008) argue that size sorting due to unidirectional and directional shears is primarily responsible for the unique  $Z_{DR}$  arc signature found in the polarimetric data collected from many supercell storms, while the size sorting process cannot be properly handled with SM schemes (Milbrandt and Yau, 2005a). Many other studies have also shown that the PSD parameters, in particular the intercept parameters, can assume a wide range of values within observed precipitation systems (e.g. Joss and Waldvogel, 1969; Houze *et al.*, 1979; Lo and Passarelli, 1982; Cifelli *et al.*, 2000; Gilmore *et al.*, 2004).

The rapid increase in computing capabilities is enabling the use of finer-resolution models and more complex microphysics schemes for explicit convective storm prediction. MM schemes have been developed since the mid-nineties that predict additional moments, allowing more parameters in the PSD functions to change freely so as to overcome certain fundamental limitations of SM schemes (e.g. Koenig and Murray, 1976; Ferrier, 1994; Ferrier *et al.*, 1995; Milbrandt and Yau, 2005a, 2005b; Morrison *et al.*, 2005). The sensitivity experiments of Milbrandt and Yau (2006) and the studies of Dawson *et al.* (2007, 2010) using the MM schemes of Milbrandt and Yau (2005a, 2005b) (the MY scheme hereafter) suggest that the double-moment (DM) and triple-moment (TM) schemes produce much more realistic storm structures than SM schemes, and most improvement is obtained

when moving from the SM to the DM scheme. This is substantiated by the results of Jung *et al.* (2010b, JXZ10b hereafter) that showed that the SM option of the MY scheme fails to simulate polarimetric signatures such as  $Z_{DR}$  arc and mid-level  $Z_{DR}$  and  $\rho_{hv}$  rings, which are, however, reproduced well by a radar simulator using DM model output. These studies suggest that MM simulations are much more realistic.

A full DM/TM scheme doubles/triples the number of microphysical state variables that a forecast model predicts. In the MY scheme, there are six cloud microphysical species, i.e. the cloud water, rain water, pristine ice crystals (ice), large crystals/aggregates (snow), graupel and hail. For the TM option, total number concentration, mass mixing ratio and reflectivity factor are predicted for each species except for cloud water where only the first two moments are predicted; there are therefore 17 prognostic microphysical variables. The increased number of state variables makes the initialization of a prediction model much more challenging while with conventional Doppler radars reflectivity is the only measured parameter that is directly related to microphysical state. Polarimetric radars provide additional parameters but the areal coverage of significant polarimetric signatures can be limited. While perfect-model OSSEs of TX05 showed that the EnKF method is able to accurately estimate the mixing ratios associated with a SM ice microphysics scheme, and additional OSSE studies (Tong and Xue, 2008b; Jung *et al.*, 2010a, JXZ10a hereafter) further demonstrated certain success estimating uncertain PSD parameters, it is not clear if EnKF is capable of estimating from radar observations multiple moments of microphysical PSDs that are needed for model initialization. As the first step towards answering the above question, we perform OSSEs with the MY DM scheme during data assimilation. The truth simulation uses either the DM or the TM scheme. Different forms of prediction model and observation operator errors are also considered.

The rest of this paper is organized as follows. The prediction model and the experimental design are first briefly described in section 2. The choice of the analysis quantity for number concentration and the simulation of observations for both perfect and imperfect model experiments are then discussed. Section 3 presents the OSSE results obtained with a perfect prediction model while section 4 discusses the results in the presence of forecast model error with or without observation operator error. A summary and conclusions are given in section 5.

## 2. Model and experimental design

### 2.1. Prediction model and data assimilation procedure

The prediction model used in both simulation and analysis in this study is the Advanced Regional Prediction System (ARPS: Xue *et al.*, 2000, 2001, 2003), which was also used in the aforementioned EnKF OSSE studies (with an SM scheme). With the DM option of the MY scheme, ARPS predicts three velocity components  $u$ ,  $v$  and  $w$ ; potential temperature  $\theta$ , pressure  $p$ , mixing ratios of water vapour  $q_v$ , and mixing ratios of cloud water, rain water, ice, snow and hail ( $q_c$ ,  $q_r$ ,  $q_i$ ,  $q_s$  and  $q_h$ , respectively) and their total number concentrations ( $N_{tc}$ ,  $N_{tr}$ ,  $N_{ti}$ ,  $N_{ts}$  and  $N_{th}$ , respectively). The shape parameter in the gamma PSDs used in the MY scheme is assumed to be zero for all categories in this study for the

DM scheme; the PSDs then become the exponential PSDs used in SM schemes. The graupel category in the original MY package is turned off to maintain consistency with our earlier studies based on the Lin *et al.* (1983) microphysics scheme (Jung *et al.*, 2008b, hereafter JXZS08; JXZ10a); this suppresses the conversion from snow to graupel by riming and from graupel to hail. The direct riming of snow to hail could be added for more accuracy, but it is not done in this study. We believe this should not affect the main proof-of-concept goal of this paper, that is, to estimate state variables associated with a MM scheme.

The configurations of the OSSEs are largely inherited from JXZS08 and JXZ10a, with some modifications to be presented later in this section. A truth simulation is created for a supercell storm whose environment is defined by the sounding of the 20 May 1977 Del City, Oklahoma, supercell storm (Ray *et al.*, 1981) and the storm in the simulation is triggered by a thermal bubble. The ensemble square-root filter (EnSRF) algorithm after Whitaker and Hamill (2002) is employed as in all of our previous EnKF studies except for TX05. A full description of the filter implementation can be found in XTD06 (see section 2). The assimilation of reflectivity at horizontal polarization ( $Z_H$ ) and radial velocity ( $V_r$ ) starts at 25 min of model time and is repeated at 5 min intervals until 100 min.

Some modifications to the configurations of the prediction model and assimilation system were made to accommodate the use of the DM scheme. First of all, the forward observation operator developed in Jung *et al.* (2008a, hereafter JZX08) for  $Z_H$  (see Eqs. (10) and (12)) is modified to use both mixing ratios and total number concentrations of rain water, snow and hail as input variables while in the original operator the number concentration depends on the specified fixed intercept parameters. The horizontal grid spacing is 1.5 km instead of the 2 km used in some of our earlier experiments, to improve the realism of storm splitting with the DM scheme. The model domain size is adjusted to 63 km  $\times$  63 km  $\times$  16 km. Constant winds of  $u = 1 \text{ m s}^{-1}$  and  $v = 13 \text{ m s}^{-1}$  are subtracted from the original sounding to keep the primary storm cell near the domain centre. Eighty ensemble members are used in all experiments. Our earlier OSSE studies with an SM scheme typically use fewer ensemble members (e.g. XTD06 and JXZS08); the larger ensemble is deemed necessary when estimating many more state variables. The filter uses a covariance localization radius of 4.5 km, determined based on experience with earlier experiments. The multiplicative inflation initially proposed by Anderson (2001) and modified by TX05 is used, which increases the ensemble spread by multiplying the ensemble perturbations by a factor greater than 1 in regions within and close to observed precipitation echo. The covariance inflation factor used in each experiment is shown in Table I.

Table I. List of OSSEs assuming a perfect model.

Experiment	Observation(s) assimilated	Covariance inflation
EXP-Vr	$V_r$ ( $Z_H > 10 \text{ dBZ}$ )	7%
EXP-Zh	$Z_H$ (everywhere)	20%
EXP-VrZh	$V_r$ ( $Z_H > 10 \text{ dBZ}$ ) and $Z_H$	20%

Using a procedure described in Tong and Xue (2008a), spatially smoothed stochastic perturbations with a horizontal correlation scale of 4.5 km are added to the initially horizontally homogeneous first guess defined by the Del City sounding to initialize the initial ensemble at 20 min model time. Perturbations are added to  $u$ ,  $v$ ,  $w$ ,  $\theta$  and  $q_v$  in the entire domain and to mixing ratios  $q_c$ ,  $q_r$ ,  $q_i$ ,  $q_s$  and  $q_h$  at the grid points located within 6 km of significant observed reflectivity (where  $Z_H$  exceeds 10 dBZ). The standard deviations of those perturbations are  $2 \text{ m s}^{-1}$ , 2 K and  $0.6 \text{ g kg}^{-1}$ , and  $0.6 \text{ g kg}^{-1}$ , respectively.

To maintain a degree of consistency with the mixing ratios, the initial total number concentrations of rain water, snow and hail are diagnosed from their perturbed mixing ratios using the default intercept parameter values of the MY SM scheme ( $1.0 \times 10^6 \text{ m}^{-4}$ ,  $1.0 \times 10^7 \text{ m}^{-4}$ , and  $1.0 \times 10^5 \text{ m}^{-4}$ , respectively) while the initial  $N_{tc}$  is set to  $1.0 \times 10^8 \text{ m}^{-4}$ , and the initial  $N_{ti}$  is a function of temperature following Cooper (1986),

$$N_{ti, \text{Cooper}} = 0.005 \exp\{0.304(T_0 - T)\}, \quad (4)$$

where  $T_0 = 273.15 \text{ K}$  and  $T$  is the ambient temperature in K.

The fields of the truth storm at 250 m altitude are shown in Figure 1(a)–(d). Briefly, the updraught quickly intensifies during the first 20 min (not shown), and the forward flank reflectivity region continues to expand with time. Storm splitting starts at around 1 hour in the simulation (Figure 1(b)), later than the SM case, presumably related to the weaker cold pool associated with the DM scheme. The left-moving cell (relative to the environmental shear vector) becomes completely separated from the right-moving cell at the low levels by 80 min, when the storm system is at its mature stage. The left-moving cell continues to grow in size and propagates towards the northwest of the right-moving cell, while the right-moving cell maintains its intensity for the next few hours. The time evolution of this truth simulation is somewhat different from that obtained using the Lin *et al.* (1983) SM scheme employed in our previous studies.

## 2.2. Transform of the total number concentration in the filter

A logarithmic transform such as  $10\log(x)$  or  $\ln(x)$  has been used in data assimilation to reduce the dynamic range of data and/or to avoid creating negative values for positive-definite variable  $x$  in the final analysis (e.g. Hogan, 2007; Tong and Xue, 2008a; JXZ10a). The drawback of the logarithmic transform is that it decreases its sensitivity with increasing value. As a result, a small overestimation (or underestimation) in the log domain can lead to a large error in the physical domain when the value of a variable subject to the estimation is very large. This necessitated the application of upper and lower bounds in the parameter estimation in JXZ10a to prevent large deviations in the early assimilation cycles that can lead to solution divergence. However, applying the upper and lower bounds is not appropriate in the estimation of  $N_t$  because they can be as small as zero and their exact upper limit is unknown. Therefore, we choose to use the power of  $N_t$  where the power is smaller than 1 so that the sensitivity at large values is retained while reducing the dynamic range of data. The choice of the power is experimentally determined and is set to 0.4 for all species in this study. The control variables

estimated in the filter are therefore  $(N_{tx})^{0.4}$ , where  $x$  denotes one of the microphysical species.

## 2.3. Simulation of observations

Two sets of simulated reflectivity observations are created in this study. For the perfect model experiments, model state variables of the truth simulation are first converted to reflectivity at model grid points using the forward observation operator of JZX08 modified to use the total number concentrations available with the DM scheme. For efficiency, this operator combines the power-law fitting of the scattering amplitudes of rain calculated using the T-matrix method (Waterman, 1969; Vivekanandan *et al.*, 1991); the scattering amplitudes of rain computed using T-matrix codes at a uniform drop size interval is fitted to a power-law function of the drop size. For ice, the Rayleigh scattering approximation is used.

Vertical beam pattern weighting (XTD06) is then performed to obtain observations on the radar elevation level. The effective Earth radius model (Doviak and Zrnić, 1993) is used to determine the beam elevation at different radar ranges. Finally, simulated errors following Xue *et al.* (2007) are added to error-free observations. As in JXZ10a, we discard error samples larger than 10 dBZ (in practice, such observations are usually discarded by quality-control procedure). The standard deviation (SD) of the relative error in equivalent reflectivity (cf. Xue *et al.*, 2007) is set to 42.7%, resulting in an effective error SD of about 2 dBZ for  $Z_H$ . We lower the maximum fraction of rain water existing in the rain–hail mixture form,  $F_{\text{max}}$ , to 0.3 from the 0.5 used in JZX08 to mitigate unrealistically high reflectivity due to the Rayleigh scattering assumptions. Gaussian errors with zero mean and SDs of  $1 \text{ m s}^{-1}$  are added to the truth  $V_r$  calculated following (3) of JXZS08.

To examine the effect of model error, we create another set of observations from a storm simulation that uses the MY TM scheme and with a more sophisticated radar simulator developed in JXZ10b. Briefly, this simulator numerically integrates over size the scattering amplitudes calculated using the T-matrix method for both rain and ice, instead of using power-law fitting of scattering amplitudes for rain and Rayleigh assumptions for ice. Also, a revised axis-ratio relation based on the observations for rain (Brandes *et al.*, 2002) is used in the simulator, but the observation operator used in the filter uses the ratio based on the equilibrium model of Green (1975). When this set of observations are assimilated using the DM scheme in the filter, we are therefore dealing with two sources of model error: (1) error originating from misrepresentation of PSDs in the prediction model and observation operator and the different treatment of associated processes in the prediction model, and (2) error in the forward observation operator due to the differences in the scattering calculation method.

## 3. Perfect-model experiments

### 3.1. Root-mean-square errors of analyses

Table I lists the set of the assimilation experiments presented in this subsection. Three experiments, which assimilate  $Z_H$  and  $V_r$  individually or together, are conducted under the perfect-model assumption. The experiment names are self-descriptive. For example, experiment EXP-VrZh assimilates

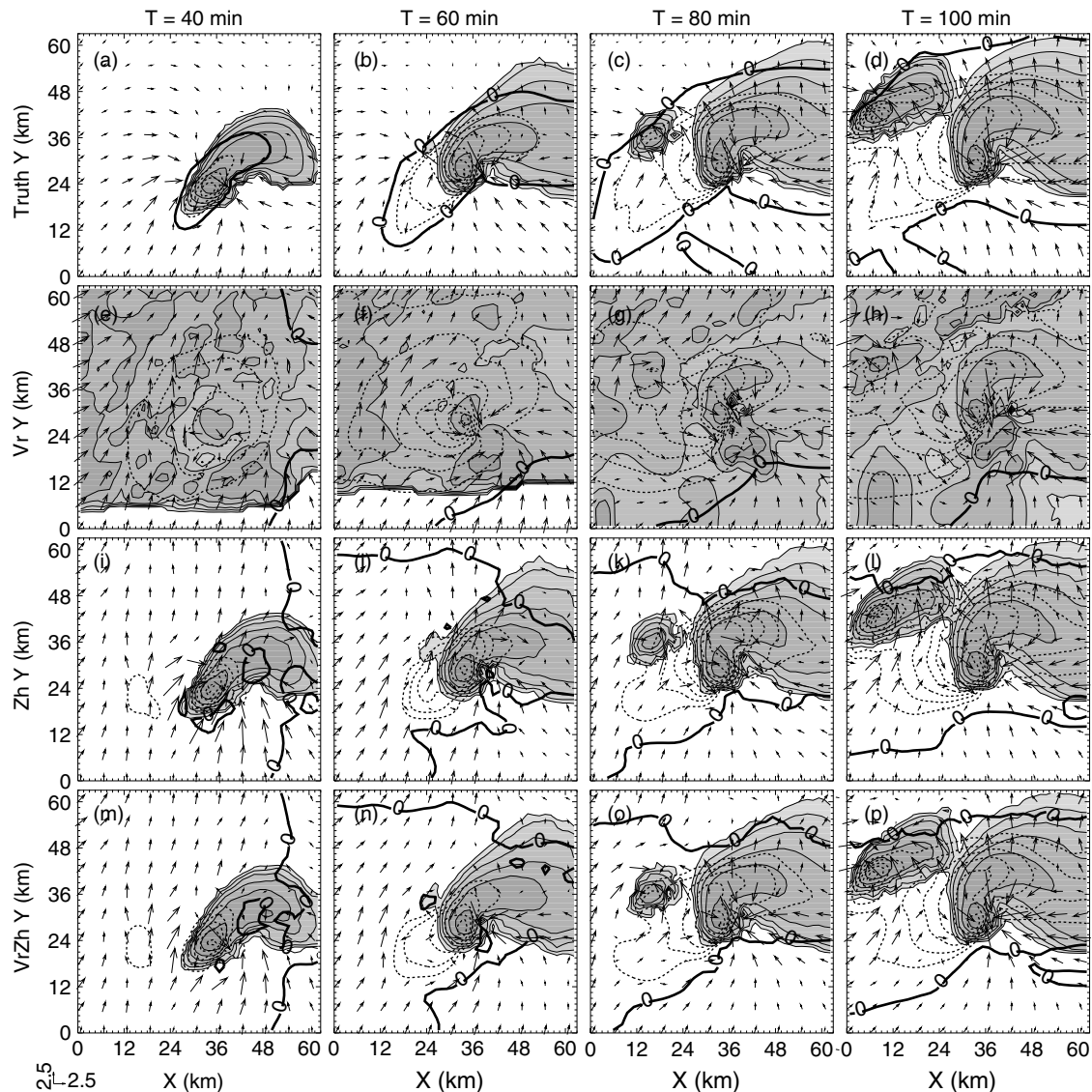


**Figure 1.** The perturbation (from environmental sounding) horizontal wind vectors ( $\text{m s}^{-1}$ , plotted every fourth grid point), perturbation potential temperature (thick black lines for 0 K and dotted contours at 0.5 K intervals for negative values) and simulated reflectivity (shaded solid contours at 10 dBZ interval, starting from 10 dBZ) at  $z = 250$  m at 40, 60, 80 and 100 min of a supercell storm: (a)–(d) truth simulation, EnKF analyses of (e)–(h) EXP-Vr, (i)–(l) EXP-Zh; and (m)–(p) EXP-VrZh.

both  $V_r$  and  $Z_H$  data, while EXP-Vr assimilates only  $V_r$  data. TX05 showed that the assimilation of clear-air reflectivity helps suppress spurious cells in echo-free regions. Therefore, reflectivity data within the entire radar coverage are assimilated, while radial velocity data are assimilated only where  $Z \geq 10$  dBZ, as in the previous studies (e.g. TX05; XTD06; JXZS08; JXZ10a). All model state variables are updated by the filter when we assimilate  $Z_H$  and/or  $V_r$ . The multiplicative inflation factors are 7%, 20% and 20% for EXP-Vr, EXP-Zh and EXP-VrZh, respectively and they were found to be optimal through experimentation.

In Figure 1, the analysed near-surface horizontal winds and potential temperature, together with the simulated reflectivity from analysed hydrometeors, from EXP-Vr, EXP-Zh and EXP-VrZh, are compared with their truth at 20-minute intervals, starting from 40 min. The fields shown are the ensemble mean. When radial velocity is assimilated alone (Figure 1(e)–(h)), spurious echoes are widespread and cannot be suppressed by the radial velocity data which are only available where the truth  $Z_H \geq 10$  dBZ. These spurious echoes quickly develop in the model integration from the

initial perturbations and they survive through assimilation cycles. With a DM scheme, a low mixing ratio can produce high reflectivity if the total number concentration is low enough. In fact, the relatively high reflectivity values in the echo-free regions in Figure 1(e)–(h) are mostly associated with very low mixing ratios (see Figure 4). In EXP-Vr, the reflectivity and cold-pool structures are poorly estimated in the echo-free region throughout the analysis cycles. However, the structure of reflectivity near the core and forward-flank precipitation regions is analysed reasonably well at the later times of the assimilation (Figure 1(g)–(h)). The shape and strength of estimated cold-pool cores of both left- and right-moving cells and the location and orientation of the gust front generally agree with those of the truth at 100 min.

When reflectivity is assimilated alone (Figure 1(i)–(l)), reflectivity data in the clear-air region effectively suppresses the spurious echoes in the first couple of cycles (not shown). The analysed reflectivity pattern is almost as good as that of EXP-VrZh which uses both  $V_r$  and  $Z_H$  data (Figure 1(m)–(p)) and is very close to the

truth (Figure 1(a)–(d)). The general cold-pool pattern matches that of truth, although the strength tends to be overestimated, and the centre of the cold pool is off by a couple of kilometres for each of the cells.

The analysed cold pool and wind fields of EXP-VrZh (Figure 1(m)–(p)) show the best match to the truth among EXP-Vr, EXP-Zh and EXP-VrZh. Improvement over EXP-Zh is clear in and around the left-moving storm in the wind fields and in the location and strength of the cold pool after 80 min.

In general, surface convergence in the updraught region and divergence in the forward-flank downdraught (FFD) region are well captured in all three experiments. The analysed wind directions and speeds are reasonable compared to the truth in the echo region, while the wind analysis at the northwest and southwest corners of the domain is rather poor, where no wind observation is available.

Figure 2 shows the ensemble mean forecast and analysis root-mean-square errors (RMSEs) of model state variables during the assimilation cycles of EXP-Vr, EXP-Zh and EXP-VrZh, averaged over the grid points where truth reflectivity is greater than 10 dBZ. In other words, the echo-free region is not included in the RMSE calculations because we are most interested in the analysis of the storm itself. For total number concentrations, RMSEs are expressed in terms of the control variables,  $(N_{tx})^{0.4}$ , where  $x$  can be  $c$ ,  $r$ ,  $i$ ,  $s$  or  $h$ . Under the perfect model assumption, the solid curves in Figure 2 show that the filter successfully reduces the RMSEs when using both reflectivity and radial velocity data. These results suggest that the filter is able to develop reliable error covariance among the large number of state variables in this situation. The final RMSE levels are comparable to those shown in Fig. 3 of JXZS08, which used an SM scheme with 40 ensemble members, although the error reduction rates are generally slower than those of Fig. 3 of JXZS08. The RMSEs of  $u$  and  $v$  drop below  $1 \text{ m s}^{-1}$  around  $t = 50 \text{ min}$  and reach below  $0.7 \text{ m s}^{-1}$  at the end, while the RMSE of  $w$  reaches about  $0.3 \text{ m s}^{-1}$ . The final RMSEs of mixing ratios are below  $0.05 \text{ g kg}^{-1}$  for  $q_c$ ,  $q_r$ ,  $q_i$  and  $q_s$ , about  $0.08 \text{ g kg}^{-1}$  for  $q_h$ , and around  $0.26 \text{ g kg}^{-1}$  for  $q_v$ . The RMSEs for  $N_{tc}$ ,  $N_{tr}$ ,  $N_{ti}$ ,  $N_{ts}$  and  $N_{th}$  in the linear domain are at the end about  $4.6 \times 10^5$ ,  $0.186$ ,  $6.89 \times 10^3$ ,  $91.9$ , and  $0.177 \text{ m}^{-3}$ , respectively. These are all several orders of magnitude smaller than their dynamic ranges; they are  $O(3)$ ,  $O(4)$ ,  $O(5)$ ,  $O(2)$ , and  $O(4)$  smaller for  $N_{tc}$ ,  $N_{tr}$ ,  $N_{ti}$ ,  $N_{ts}$  and  $N_{th}$ , respectively. The rain water reaps the largest benefit from the assimilation for both mixing ratio and total number concentration.

When reflectivity is assimilated alone, the filter is still able to effectively estimate the state variables in the DM case (Figure 2), although the RMSEs at the end of assimilation cycles are larger than those of a similar SM experiment reported in JXZS08 (solid black in their Fig. 3). The lower accuracy is expected due to the increased degree of freedom. In the DM case, even when only one hydrometeor species exists, reflectivity alone cannot uniquely determine both mixing ratio and total number concentration. Additional  $V_r$  observations are apparently very helpful. Figure 1 shows that the analysed reflectivity (which is the assimilated quantity) in EXP-Zh is almost as good as that of EXP-VrZh, but the RMSEs of state variables in EXP-Zh (dashed line in Figure 2) are generally two or three times larger than those of EXP-VrZh.

Radial velocity alone results in smaller RMSEs in wind variables ( $u$ ,  $v$  and  $w$ ), and in  $q_v$ ,  $q_c$  and  $N_{tc}$  than reflectivity alone does (Figure 2). The fact that the  $V_r$  observation operator is independent of the PSD may be part of the reason. At the end of the assimilation window, the analysis RMSEs of  $u$  and  $v$  are around  $1.1 \text{ m s}^{-1}$  and that of  $w$  is about  $0.7 \text{ m s}^{-1}$ . Ice category is not involved in the observation operators; its estimation, therefore, solely depends on the cross-covariance of state variables and on thermodynamic and microphysical adjustments within the prediction model. Reflectivity clearly performs better than  $V_r$  for the estimation of  $q_s$ ,  $N_{tr}$ ,  $N_{ts}$  and  $N_{th}$ , which are all directly linked to the reflectivity. These results suggest that the reflectivity data are more effective in estimating variables directly linked to reflectivity while radial velocity data are more effective for other state variables, especially for the wind components.

To examine the height dependency of the errors, Figure 3 shows the vertical profiles of the RMSEs averaged horizontally over points at which the truth reflectivity is greater than 10 dBZ for experiments EXP-Vr (dotted), EXP-Zh (dashed), and EXP-VrZh (solid) at 100 min. EXP-Vr generally outperforms EXP-Zh in terms of  $u$ ,  $v$ ,  $w$ ,  $q_v$ ,  $q_c$ ,  $q_r$  and  $N_{tc}$  at the middle to lower levels (Figure 3(a)–(c), (e)–(g), (k)). Improvements are found at all levels in all state variables when both  $V_r$  and  $Z_H$  are assimilated, compared to EXP-Zh or EXP-Vr, except for  $u$  and  $q_r$  at some limited levels.

### 3.2. Problem associated with underconstrained solution

We pointed out earlier that even though the analysed reflectivity is of similar quality in EXP-Zh and EXP-VrZh, the errors in state variables such as  $q_r$ ,  $N_{tr}$ ,  $q_s$ ,  $N_{ts}$ ,  $q_h$  and  $N_{th}$  are much larger in EXP-Zh. These state variables are directly involved in the reflectivity calculations. Given  $V_r$  or  $Z_H$  observations alone, the state estimation is underconstrained by the observations. Reflectivity is a function of the mass as well as the size distributions of rain, snow and hailstones in the atmosphere and it is used to estimate multiple hydrometeor types that often coexist. In such a case, the error in one state variable may compensate the error in other state variables, leading to larger errors in all fields involved. For illustration purposes, we assume that the atmosphere contains raindrops only. When a SM scheme is used in the OSSEs, reflectivity is solely determined by the rain mixing ratio under the assumption that the PSD of the raindrops is known. In such a case, a good fit of the analysed reflectivity to observations usually means an accurate analysis of the rain mass also in an OSSE framework. When a DM scheme is used, both rain mixing ratio and total number concentration of raindrops have to be determined from the observations; the same reflectivity can correspond to virtually unlimited pairs of  $q_r$  and  $N_{tr}$  unless other observation and/or model constraints play significant roles. While large errors may exist in  $q_r$  and  $N_{tr}$ , the filter may not see them as long as the fit of reflectivity to observations is good.

This problem is illustrated in Figure 4, which shows the  $q_r$  and  $N_{tr}$  error fields, calculated against the truth at 500 m height for EXP-Vr, EXP-Zh and EXP-VrZh. At this level, rain water is dominant, so the estimation problem is actually simpler. When reflectivity is assimilated alone (Figure 4(b)), the rain water mixing ratio at the precipitation core is overestimated in both left- and right-moving storms. There is also significant error in  $N_{tr}$ ; yet, the analysed

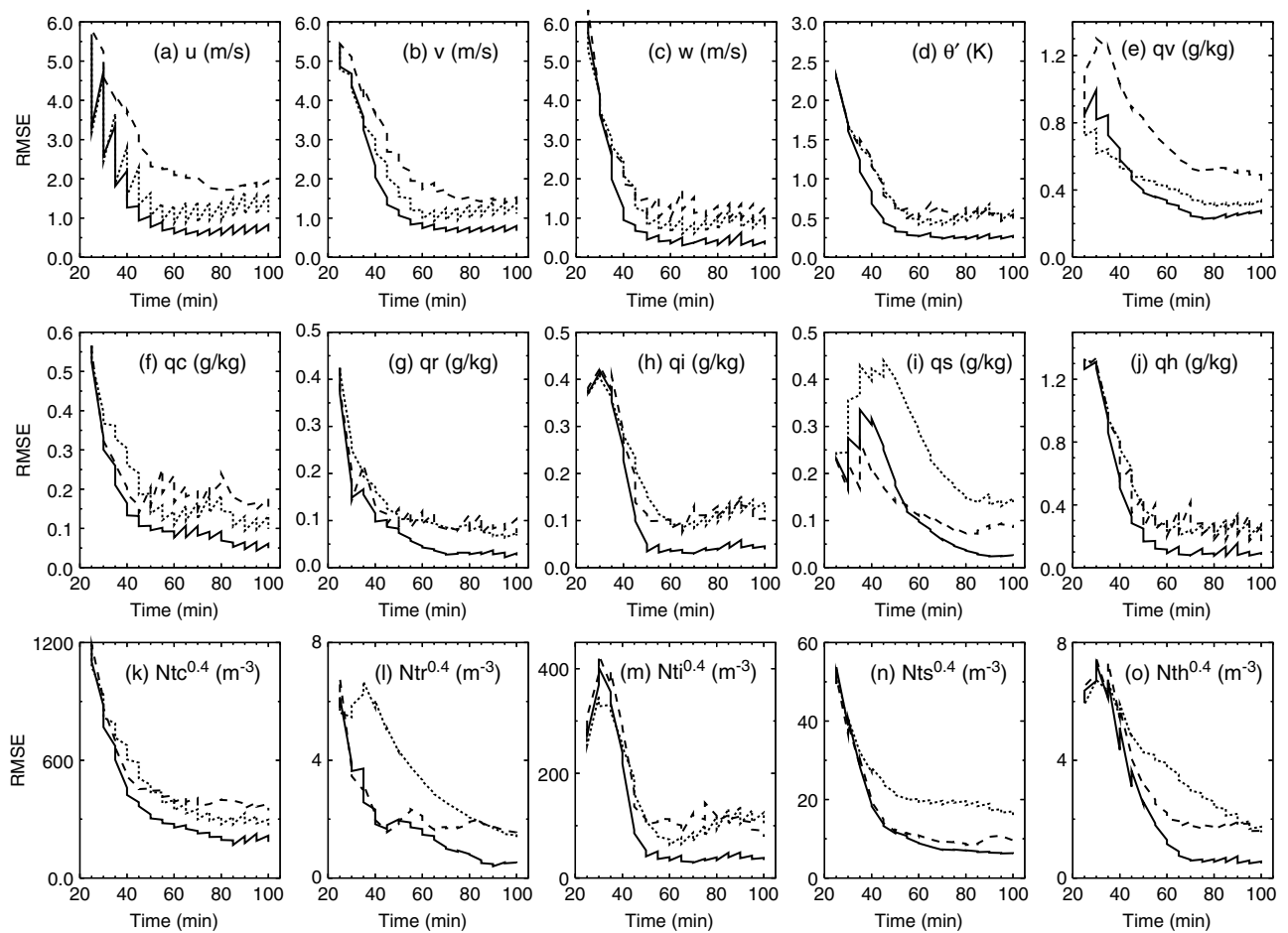


**Figure 2.** The ensemble mean forecast and analysis RMSEs averaged over points at which the true reflectivity is greater than 10 dBZ for (a)  $u$ , (b)  $v$ , (c)  $w$ , (d) perturbation potential temperature  $\theta'$ , (e)  $q_v$ , (f)  $q_c$ , (g)  $q_r$ , (h)  $q_i$ , (i)  $q_s$ , (j)  $q_h$ , (k)  $N_{tc}$ , (l)  $N_{tr}$ , (m)  $N_{ti}$ , (n)  $N_{ts}$  and (o)  $N_{th}$ , for EXP-VrZh (solid), EXP-Vr (dotted), and EXP-Zh (dashed). The vertical straight-line segments in the curves correspond to the reduction or increase in RMSEs by the filter.

reflectivity (thick solid contours) matches the truth very well (Figure 1(d)). In comparison, EXP-VrZh produces better estimates of  $q_r$  and  $N_{tr}$  than EXP-Zh (Figure 4(c)). In EXP-Vr, both  $q_r$  and  $N_{tr}$  errors are smaller than those of EXP-Zh near the reflectivity core in the right-moving cell while  $q_r$  is underestimated in the left-moving cell. The uncertainty increases when multiple species coexist. These results suggest that additional information beyond  $Z_H$  is needed to obtain good state estimation associated with MM schemes. The radial velocity data are helpful, while additional information from polarimetric radars may also help.

### 3.3. Impact of ensemble size

The use of rather small ensemble sizes relative to the total degrees of freedom of the system causes rank deficiency with the estimated covariance matrix and underestimation of error variance that can lead to filter divergence. In this study, an ensemble size of 80 is used in most experiments considering more degrees of freedom in the DM case, while earlier studies with SM schemes often use smaller ensembles (e.g. XTD06). To examine the impact of ensemble size, experiments shown in Figure 2 are repeated using 40 ensemble members.

Figure 5 shows the RMSEs and ensemble spreads of select state variables from experiment EXP-Zh run with 80 and 40 members. The degradation of the filter performance

with the smaller ensemble is observed in essentially all state variables starting from the intermediate cycles around 50 minutes. Rapid error increases are found with  $\theta'$ ,  $q_v$ ,  $q_c$ ,  $N_{tc}$ ,  $q_r$  and  $N_{tr}$  in the later cycles (Figure 5(c)–(h)), which implies filter divergence. In Figure 5, ensemble spreads of experiment with 40 members (thin dashed) are consistently smaller than those with 80 members (thin solid). Both of the above experiments used multiplicative inflation with an inflation factor of 20% (see Table I). When the inflation factor is increased to 25% in the 40-member case, the analysis quality is improved to be close to that of 80 members.

On the other hand, when  $V_r$  alone or both  $V_r$  and  $Z_H$  are assimilated with 40 ensemble members, the RMSE curves show similar error reduction trends with somewhat slower convergence rates (not shown). At the end of the assimilation window, the RMSEs are slightly larger than those of corresponding runs with 80 members but the difference between the two runs is small. These results indicate that  $V_r$  in addition to  $Z_H$  can lead to the stable estimations with 40 ensemble members when the prediction model is perfect. However, this may not be true in real-case scenarios where significant model error often exists.

### 3.4. Ensemble correlation analysis

In an EnKF system, a successful estimation of model state variables from a very limited set of observed parameters, as with radar data, depends to a larger extent on the ability of the

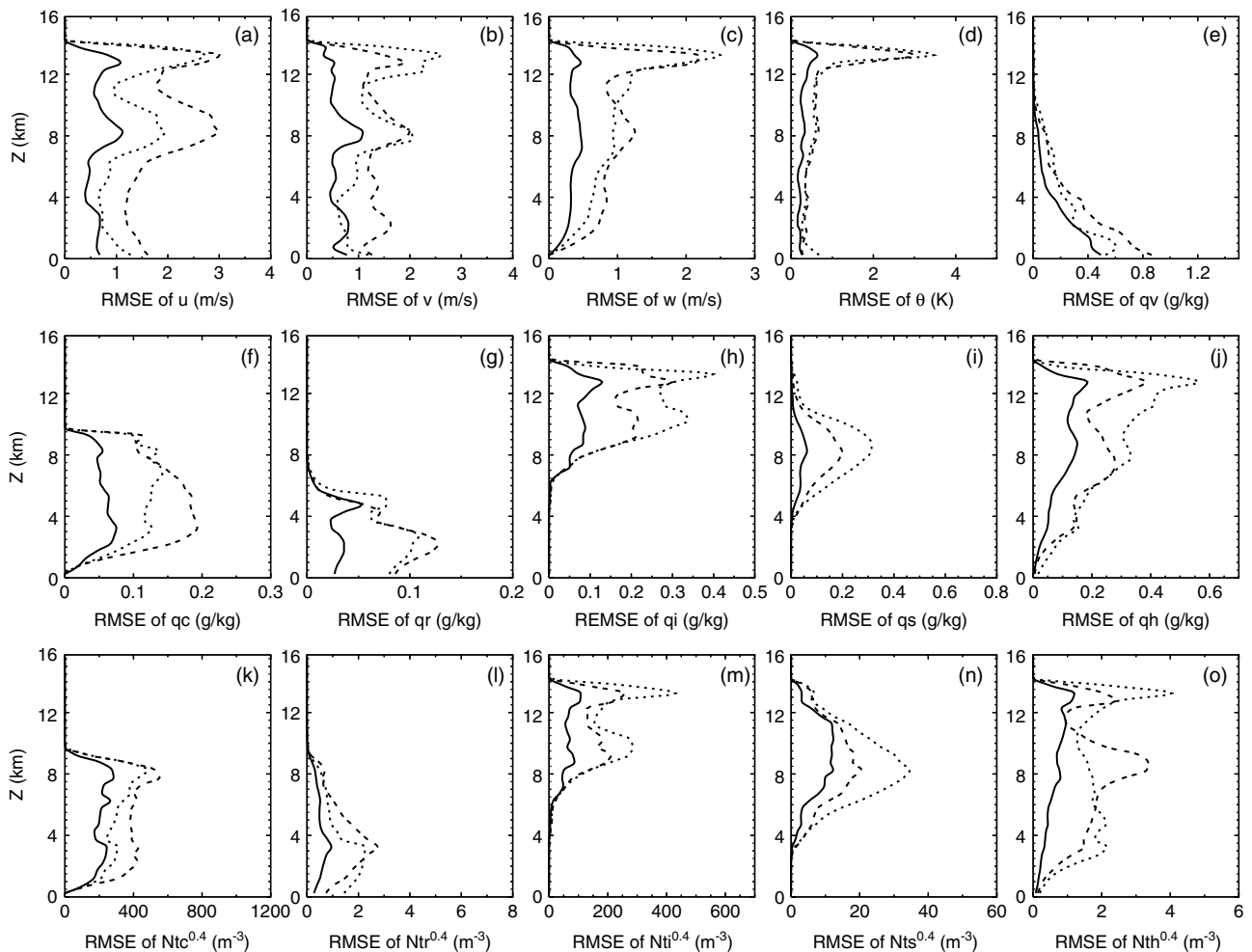


**Figure 3.** The horizontally averaged ensemble mean analysis RMSEs averaged over points at which the truth reflectivity is greater than 10 dBZ for (a)  $u$ , (b)  $v$ , (c)  $w$ , (d)  $\theta'$ , (e)  $q_v$ , (f)  $q_c$ , (g)  $q_r$ , (h)  $q_i$ , (i)  $q_s$ , (j)  $q_h$ , (k)  $N_{tc}$ , (l)  $N_{tr}$ , (m)  $N_{ti}$ , (n)  $N_{ts}$  and (o)  $N_{th}$ , for EXP-VrZh (solid), EXP-Vr (dotted), and EXP-Zh (dashed) at 100 min.

filter to develop reliable multivariate covariance through the assimilation cycles. This makes the EnKF method attractive for radar data assimilation because the variables that are not directly observed can be 'retrieved' based on the cross-covariance between the state variables and the prior estimates of observations. As an example, we show in Figure 6 the forecast error correlations between the prior estimate of reflectivity at point  $x = 38.5$  km and  $z = 8$  km and model variables at each grid point in an  $x$ - $z$  plane through the maximum updraught at  $y = 33$  km and 100 min.

With the assumed observation located near the updraught core, significant correlations are found through much of the deep updraught. Figure 6(c) shows that large negative correlation is found between  $Z_H$  and  $w$  in essentially the entire updraught region, extending from the surface up to the model top. The correlations between  $Z_H$  and  $q_r$ ,  $q_h$ ,  $N_{tr}$  and  $N_{th}$  also show negative correlations in a considerably deep layer, which includes the location of the chosen  $Z_H$  (Figure 6(a)–(b), (d)–(e)). This contrasts with the almost entirely positive correlation found in TX05 between  $w$ ,  $q_r$  and  $q_h$ , and an assumed reflectivity observation located at a 6 km height (see Fig. 5 of TX05). In both cases, the freezing level locates around 4 km altitude. Therefore, reflectivity observations are taken from where hydrometeors are mostly in the ice phase for both cases. In TX05, an SM scheme is used in the model simulations, where a stronger

updraught is expected to produce more condensation and higher reflectivity; a positive correlation between  $Z_H$  and  $w$  is expected. The negative correlation between  $Z_H$  and  $w$  found in the current case appears counter-intuitive.

This negative correlation appears to be related to the more complex and also more realistic microphysical processes that can be represented by DM schemes. The non-unique mapping between reflectivity and hydrometeor content is another factor to consider. When a DM scheme is used, the water/ice content and their total number concentrations can vary independently. The calculated reflectivity is not necessarily large when the condensate content is greater; it also depends on the number concentration. When the updraught intensity increases, supersaturation tends to increase. In this case, more cloud condensation nuclei (CCN) are activated to decrease the supersaturation and, therefore,  $q_c$  and  $N_{tc}$  increase (Figure 7(b) and (e)) (Rogers and Yau, 1989). The number of ice nuclei (IN) to be activated is also a function of supersaturation; the same theory can be applied to ice at the upper level (not shown).

With more cloud drops that can grow into rain drops at the lower to middle levels, more supercooled water  $q_r$  and  $N_{tr}$  are carried upwards by a stronger updraught (Figure 7(a) and (d)), and the number of hailstones that are converted from raindrops through freezing when temperature is below  $0^\circ\text{C}$  increases. The increase in the number concentration

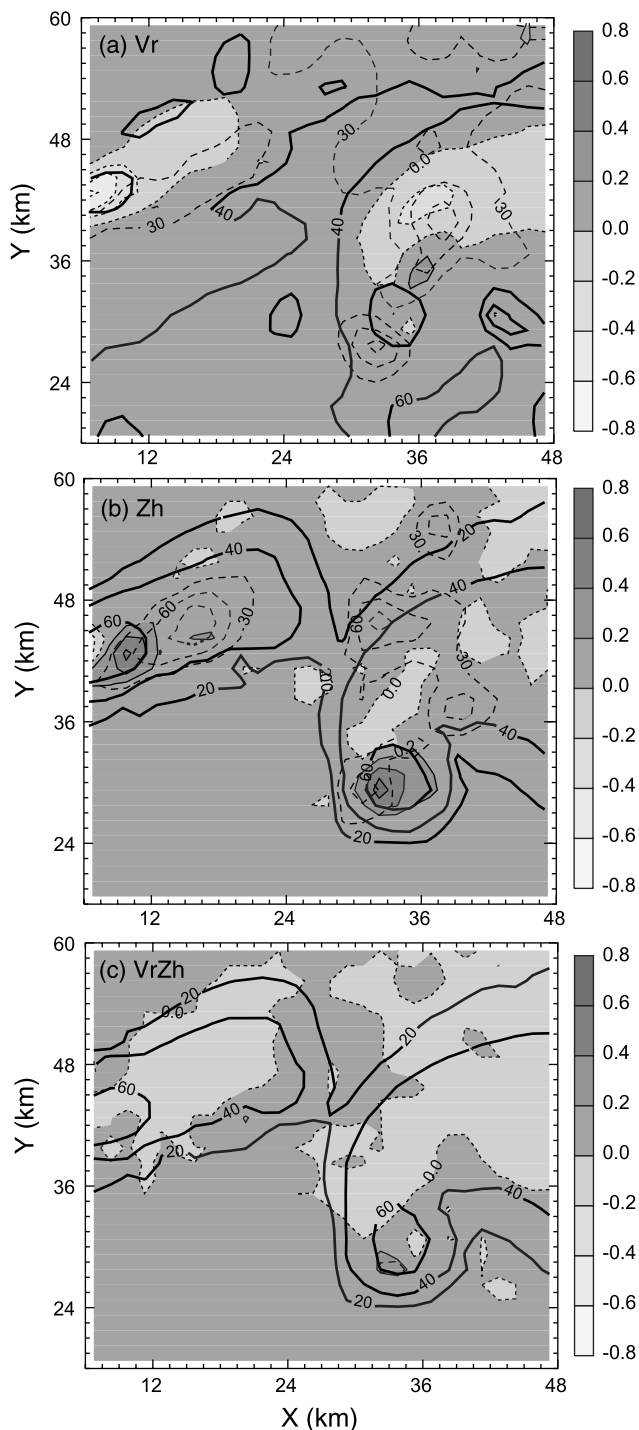


**Figure 4.** Rain water mixing ratio error ( $\text{g kg}^{-1}$ , solid contours with shading for positive and dotted contours with shading for negative), total rain water number concentration error (dashed contours at intervals of  $30 \text{ m}^{-3}$ , starting from  $0 \text{ m}^{-3}$ ), and simulated reflectivity (thick solid contours at 20 dBZ intervals, starting from 20 dBZ), at  $z = 500 \text{ m}$  and  $t = 100 \text{ min}$  for (a) EXP-Vr, (b) EXP-Zh and (c) EXP-VrZh.

of hail is also promoted by the increase in the number concentration of ice through spontaneous particle growth processes from ice to snow, snow to hail, ice to hail, etc. This is consistent with the fact that  $q_h$  and  $N_{th}$  show positive correlations with  $w$  at the upper levels (Figure 7(c) and (f)). Furthermore, an increase in the updraught speed decreases the time the ice particles have to grow as they are carried more quickly to the upper levels, and the growth by collection/coalescence is likely to be less efficient among

ice particles. For these reasons, the size spectrum of ice hydrometeors is likely shifted toward smaller sizes in a deep layer than that of weaker updraught cases. The increase in the number concentration can offset the increased amount of suspended water/ice, leading to a lower reflectivity hence negative correlation between  $w$  and  $Z$  in the updraught core region. This is consistent with the correlation patterns shown in Figure 6(a)–(b), (d)–(e). We offer this as our hypothesis for the negative correlations observed here. A detailed validation of this hypothesis would require further study.

The correlation pattern for  $\theta'$  is similar to that of  $w$  (Figure 6(f)) because they are positively correlated: the positive buoyancy is associated with stronger updraughts. The  $\theta'$  is also positively correlated with mixing ratios at this level because of the latent heat release where the mixing ratio is negatively correlated with reflectivity, as discussed above.

The correlation patterns show complex three-dimensional structures depending on the locations of observations. When the observation is taken at 4 km (Figure 8), where a significant amount of liquid exists, the correlation fields show very different patterns compared to those shown in Figure 6. The correlation for  $q_r$  is positive, while the correlation for  $N_{tr}$  is negative at the location of the observation (Figure 8(a) and (c)). This is an indication that the PSD shift toward larger particle sizes increases  $Z_H$  and that the PSD shift toward smaller particle size decreases  $Z_H$ . Stronger updraughts can sustain larger raindrops where collision and coalescence processes are more effective in drop growth than they are at upper levels, which may effectively reduce the total number concentration in the atmosphere. Therefore, the reflectivity and  $w$  show positive correlation at this level while  $N_{tr}$  and  $Z_H$  show negative correlation (Figure 8(b) and (c)). As discussed above,  $\theta'$  is positively correlated with  $w$  and  $q_r$ . Because of the complexity and nonlinear nature of microphysical processes, a full understanding of the behaviours of the SM and DM schemes will require further study.

#### 4. Imperfect-model experiment

The results of perfect-model OSSEs reported earlier can be considered rather successful, especially when both  $V_r$  and  $Z_H$  data are assimilated. In reality, numerical models and their parametrization schemes are never perfect. In the case of convective-storm simulation, microphysics parametrization is likely one of the largest sources of error. To examine the impact of model error, we performed six additional experiments as listed in Table II. In the first two experiments (VrZh\_ptr $\alpha$ \_IM and VrZh\_cst $\alpha$ \_IM), model error exists because of the use of incorrect  $\alpha$  (the shape parameter) values in the gamma PSDs for rain and hail in the prediction model, although the perfect  $\alpha$  value is used in the observation operator. In the experiment names, 'ptr $\alpha$ ' stands for 'perturbed  $\alpha$ ' and 'cst $\alpha$ ' for 'constant  $\alpha$ '. Suffix 'IM' denotes 'imperfect forecast model'. In experiment VrZh\_ptr $\alpha$ \_IM, 'perturbed' values of  $\alpha$  for rain and hail are used in the ensemble members. The  $\alpha$  for rain increases from  $-1$  to  $3$  at a constant interval of  $0.05$ , while that for hail decreases from  $3$  to  $1$  at intervals of  $0.025$  sequentially for each ensemble member, while the correct  $\alpha$  value used in the truth simulation is  $0$  for both species. The assumed uncertainty ranges are chosen based on our limited knowledge of PSDs.

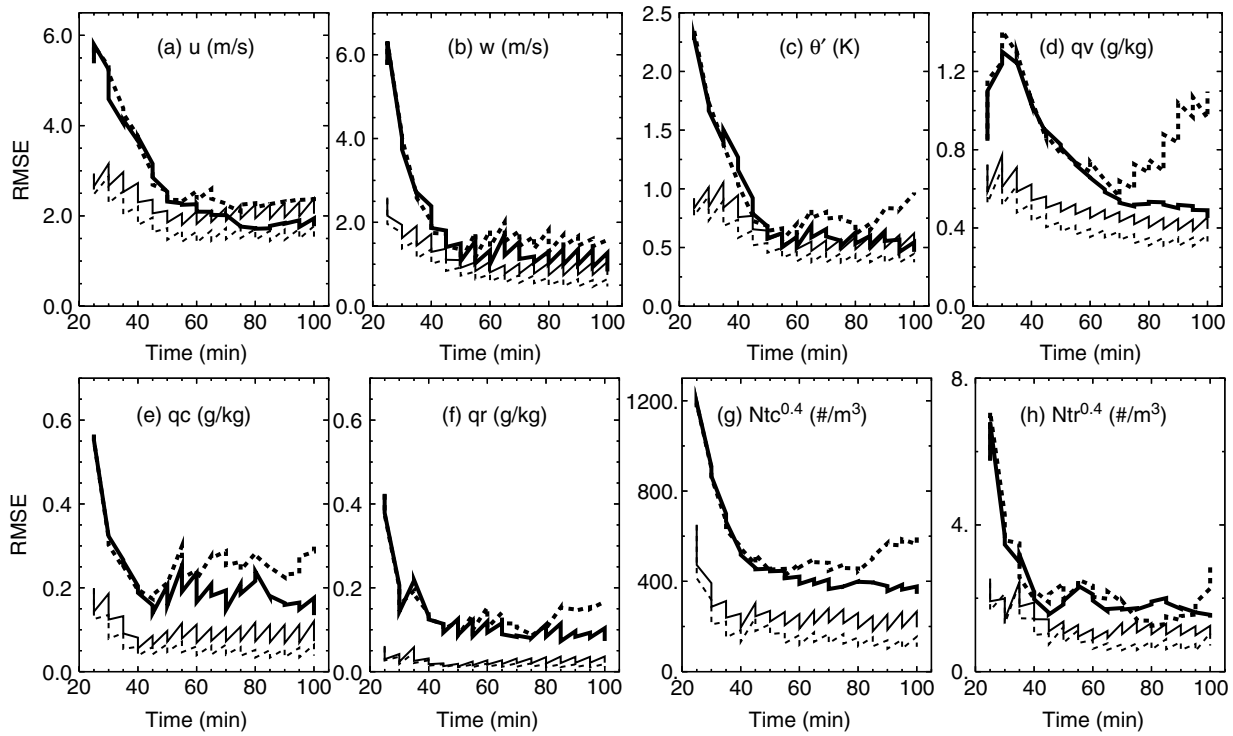


Figure 5. As in Figure 2 but for (a)  $u$ , (b)  $w$ , (c)  $\theta'$ , (d)  $q_v$ , (e)  $q_c$ , (f)  $q_r$ , (g)  $N_{tc}$  and (h)  $N_{tr}$ , for EXP-Zh run with 80 ensemble members (solid) and with 40 ensemble members (dashed). The thin curves are for the RMSEs and the thick curves are for the ensemble spread.

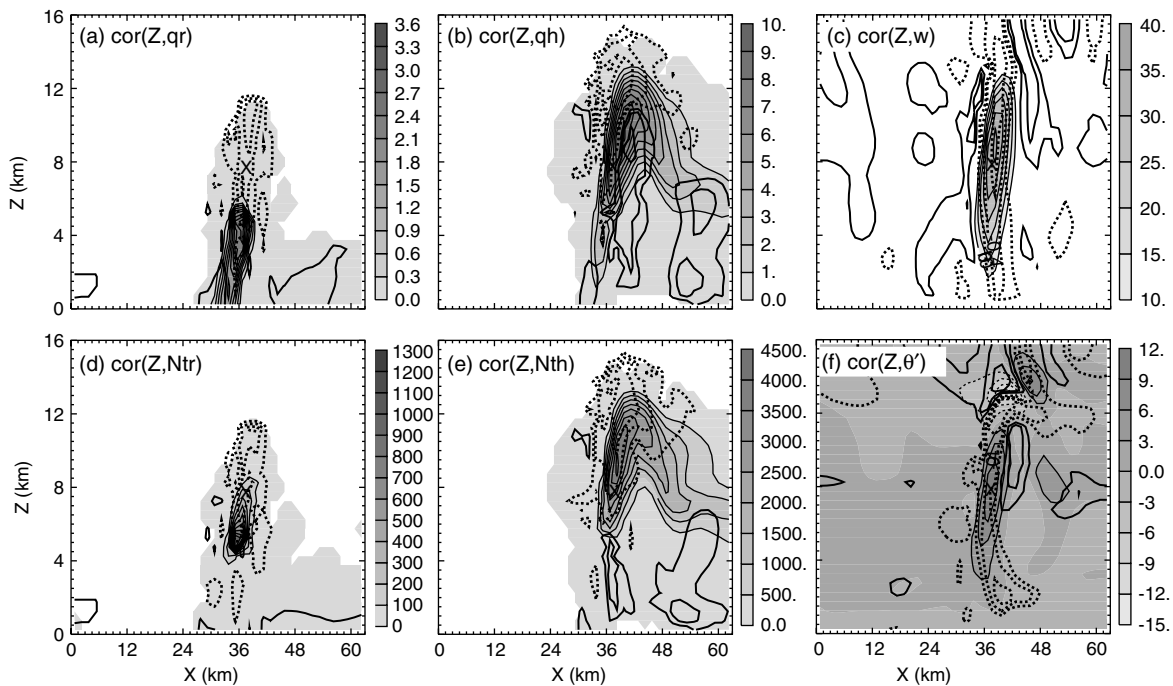


Figure 6. Forecast error correlations (thick solid and dotted contours at interval of 0.2) computed from the ensemble for EXP-VrZh at  $t = 100$  min in the  $x-z$  plane at  $y = 33$  km, which passes through the updraught core (maximum vertical velocity). Thick solid (dotted) contours represent positive (negative) error correlations between forecast reflectivity  $Z_H$  at  $x = 37.5$  km and  $z = 8$  km (indicated by the boldface X) and (a)  $q_r$ , (b)  $q_h$ , (c)  $w$ , (d)  $N_{tr}$ , (e)  $N_{th}$  and (f)  $\theta'$ . The shading and thin solid contours are model fields from the truth simulation with units of (a), (b)  $g\ kg^{-1}$ , (c)  $m\ s^{-1}$ , (d), (e)  $m^{-3}$ , and (f) K. Zero correlation lines are suppressed.

The negative  $\alpha$  for rain is less frequent but still observed in some, such as orographic, precipitation systems. Therefore, we included negative  $\alpha$  for rain. For hail, we intentionally choose a range of the perturbed  $\alpha$  values that does not include the truth value to see if perturbing  $\alpha$  can still help. In VrZh\_cst $\alpha$ \_IM,  $\alpha$  is set to constant/fixed but incorrect values of 3 and 2 for rain and hail, respectively. Rain and hail

are chosen because they affect the reflectivity measurements most. These experiments assimilate both reflectivity and radial velocity, and use the same covariance inflation factors as the corresponding perfect-model experiments discussed in section 3.

In the next four imperfect-model experiments, both forecast model and observation operator errors are

Table II. List of OSSEs with forecast model error.

Error type	Experiments	Values/configuration in DA	Truth simulation
In shape parameter ( $\alpha$ ) of gamma PSDs in forecast model	VrZh_ptr $\alpha$ _IM	$\alpha_r = -1 - 3, \alpha_h = 3 - 1$	$\alpha_r = 0, \alpha_h = 0$
	VrZh_cst $\alpha$ _IM	$\alpha_r = 3, \alpha_h = 2$	
In PSDs of both forecast model and observation operator, and in the representation of the scattering properties in observation operator	Vr_obs_IM	Exponential PSDs, Power-law fitting of T-matrix scattering for rain, Rayleigh approx. for ice species	Gamma PSDs, T-matrix scattering for all species
	Zh_obs_IM		
	VrZh_obs_IM		
	VrZh_ptr $\alpha$ _obs_IM	As in VrZh_obs_IM but with $\alpha_r = -1 - 3, \alpha_h = 3 - 0$	

In the experiment names, 'ptr $\alpha$ ' stands for 'perturbed  $\alpha$ ' and 'cst $\alpha$ ' for 'constant  $\alpha$ .' Suffix 'IM' denotes 'imperfect forecast model'.

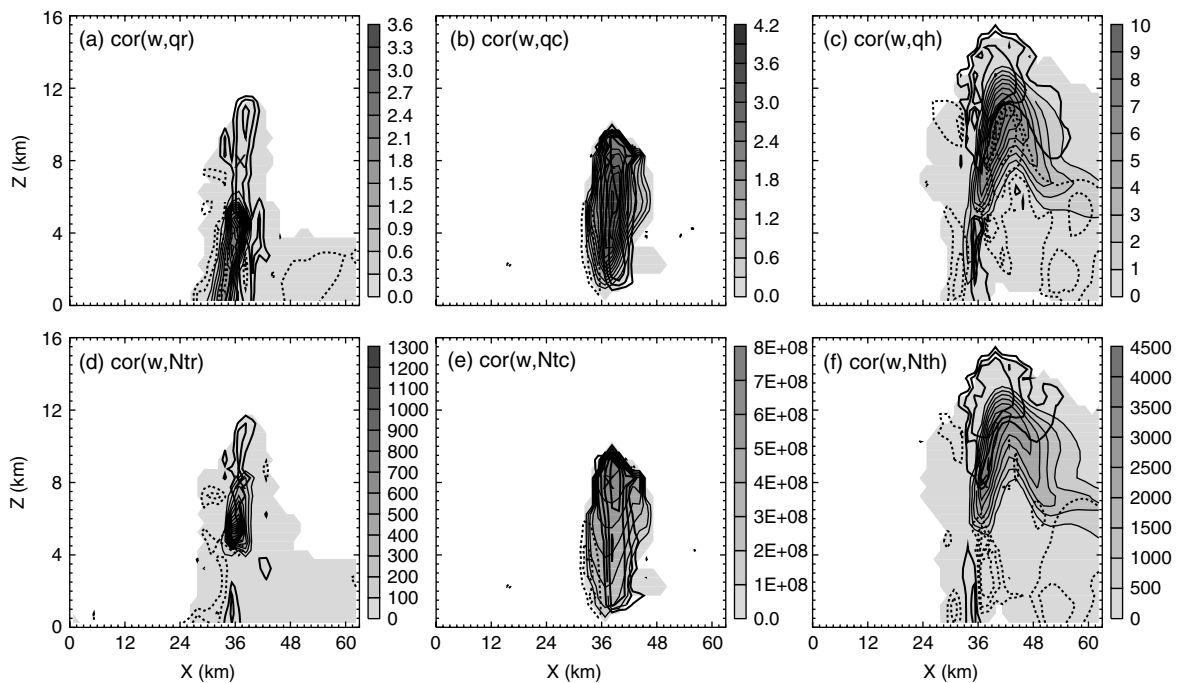


Figure 7. As in Figure 6, but between forecast  $w$  and (a)  $q_r$ , (b)  $q_c$ , (c)  $q_h$ , (d)  $N_{tr}$ , (e)  $N_{tc}$  and (h)  $N_{th}$ .

introduced. In this case, the truth simulation is created using the MY TM scheme, which effectively allows the intercept, shape and slope parameters of gamma PSDs to vary independently in time and space. Because the shape parameter is assumed zero in both prediction model and observation operators during the data assimilation, this mismatch represents a significant PSD-related model error. Furthermore, as described in section 2.3, the reflectivity observations are simulated by the radar simulator of JXZ10b with the T-matrix method for all species and a revised rain axis ratio after Brandes *et al.* (2002). The use of different scattering calculation methods represents another source of observation operator error. These four experiments assimilate  $V_r$  or  $Z_H$  only or both (Table II). Characters 'obs' in the experiment names denote 'imperfect-observation operator'. These experiments are otherwise the same as those listed in Table I that use the perfect-observation operator.

#### 4.1. Experiments with forecast model error only

Figure 9 shows the ensemble mean forecast and analysis RMSEs of state variables during the assimilation cycles of experiments VrZh\_cst $\alpha$ \_IM and VrZh\_ptr $\alpha$ \_IM. The RMSEs show rapid reduction in the first few cycles, at rates very similar to those of the control experiment without model error. When each ensemble member uses the same incorrect  $\alpha$  values in VrZh\_cst $\alpha$ \_IM (thick solid grey), the error reduction is generally slower than the control between 40 to 60 min, and the errors stay noticeably higher than those of the control experiment for all state variables except for  $q_v$ , whose error is similar to that of control. The state variables directly related to the incorrect PSD parameters show far larger errors than the rest of the variables: the errors in  $q_r$ ,  $N_{tr}$ ,  $q_h$  and  $N_{th}$  are about 135%–500% larger than those of the control experiment, while errors of other variables are about 10%–110% larger.

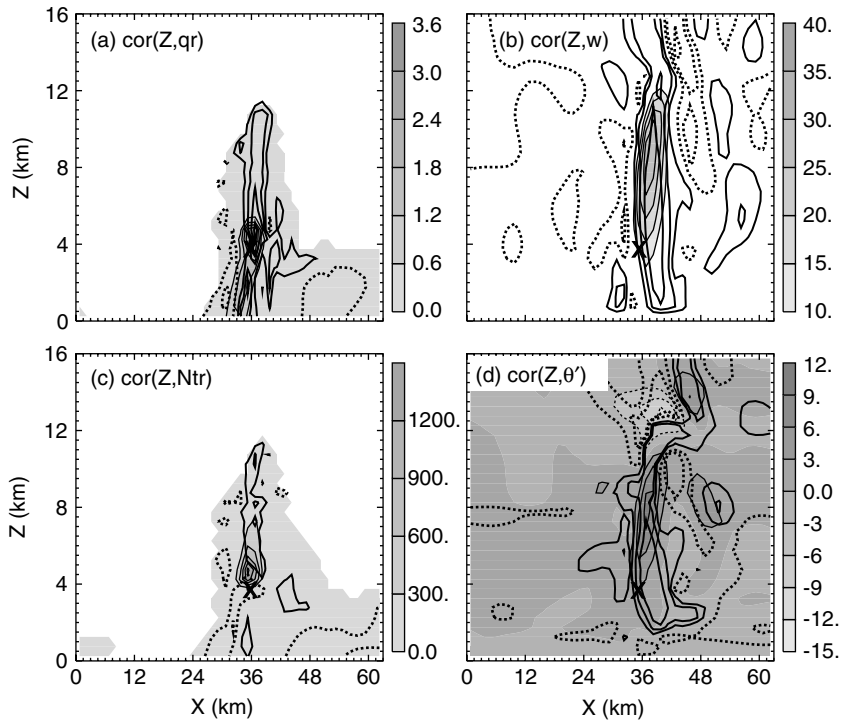


Figure 8. As in Figure 6, but correlations between forecast reflectivity  $Z_H$  at  $x = 36$  km and  $z = 4$  km and (a)  $q_r$ , (b)  $w$ , (c)  $N_{tr}$  and (f)  $\theta'$ .

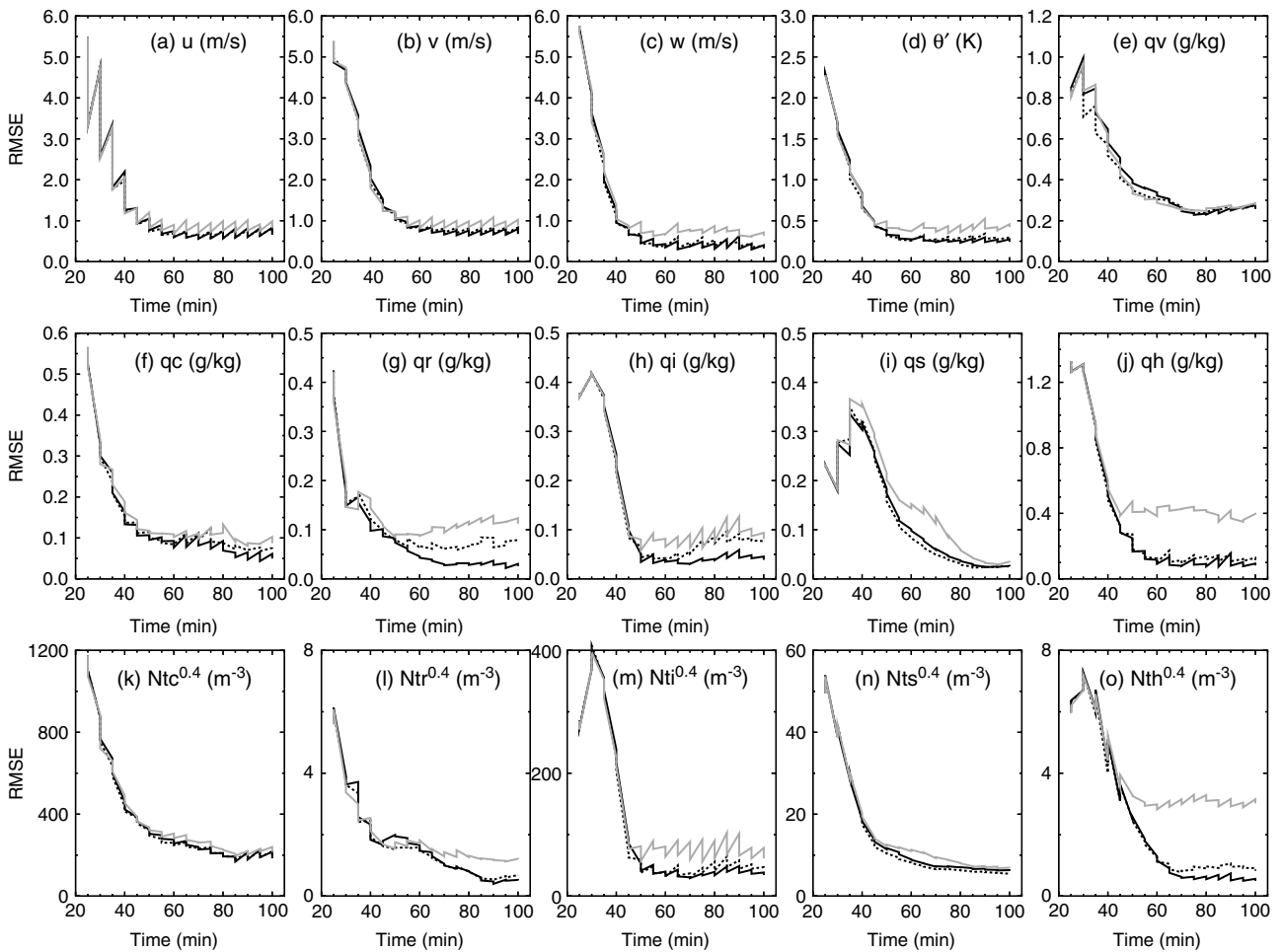


Figure 9. As in Figure 2, but for experiments VrZh-ptra\_IM (thin dotted black) and VrZh-csta\_IM (thick solid grey). The RMSEs of control run EXP-VrZh, with  $\alpha_r = \alpha_h = 0$ , are shown in thin solid black for comparison.

In VrZh\_cst $\alpha$ \_IM, the RMSEs of  $u$ ,  $v$  and  $w$  are less than  $1 \text{ m s}^{-1}$ , and those of  $q_c$ ,  $q_i$  and  $q_s$  are less than  $0.1 \text{ g kg}^{-1}$ , with that of  $\theta'$  being less than  $0.5 \text{ K}$ . The RMSEs of  $N_{tc}$ ,  $N_{ti}$  and  $N_{ts}$  are also 2–4 orders of magnitude smaller than their respective dynamic ranges. Considering the generally low errors in the later cycles after the RMSEs stabilize, the 10%–110% increase in error may be insignificant. This result suggests that the impact of incorrect shape parameters on those state variables not directly related to these parameters is relatively small.

When each member is assigned an  $\alpha$  value in a certain range that does not centre on the true value, for both rain and hail, the state estimation is actually rather close to that of control (dotted line in Figure 9); the RMSEs of most state variables are almost as low as those of control experiment EXP-VrZh (black solid line in Figure 9). Those of  $q_r$  and  $q_i$  are two exceptions; they are about two times larger than in control. It is interesting that  $q_h$  and  $N_{th}$  are estimated rather accurately, even though the true value of 0 for  $\alpha_h$  is outside the range of 1 and 3 used in the ensemble members.

Several past studies showed that employing different parameterization schemes in different ensemble members improves analysis (e.g. Meng and Zhang, 2007). When  $\alpha_r$  and  $\alpha_h$  are perturbed in the ensemble members, the ensemble spreads of  $q_r$ ,  $N_{tr}$ ,  $q_h$  and  $N_{th}$  increase compared with those of the control experiment. In the later cycles, the ensemble spreads of  $N_{tr}$ ,  $q_h$  and  $N_{th}$  are close to the level of their RMSEs, while the spreads in VrZh\_cst $\alpha$ \_IM are found to be even lower than their corresponding ones in control (not shown). The results suggest that when faced with model parameter uncertainty, using perturbed values is much better than using a single incorrect value in the ensemble members, even though the perturbed values might not centre on the right value.

#### 4.2. Experiments with both forecast model and observation operator errors

In this subsection, we examine the impact of observation operator error and a different form of model error on the EnKF analysis. In experiments VrZh\_obs\_IM, Vr\_obs\_IM and Zh\_obs\_IM that assimilate  $V_r$  and  $Z_H$ ,  $V_r$  alone and  $Z_H$  alone, respectively, the truth simulation uses the MY TM scheme and the data are simulated using an independent radar emulator; this scenario is more realistic than those of earlier experiments. The RMSEs of the state variables shown in Figure 10 are calculated against the truth simulation.

Although the reflectivity data in Zh\_obs\_IM noticeably reduce the errors in most state variables (Figure 10), the final errors are much higher than those obtained in the perfect-model scenarios (Figure 2). For example, the RMSEs of  $u$  and  $v$  are about  $3 \text{ m s}^{-1}$ , that of  $w$  around  $2 \text{ m s}^{-1}$ , and those of mixing ratios all greater than  $0.1 \text{ g kg}^{-1}$ . A tendency of rapid RMSE decrease in the first 4–6 cycles, followed by error increase, is found in many of the microphysical variables, including  $q_c$ ,  $q_r$ ,  $q_i$ ,  $N_{tc}$ ,  $N_{tr}$ ,  $N_{ti}$ ,  $N_{ts}$  and  $N_{th}$ . In the current OSSE framework, only microphysical variables are directly involved in the observation operators; the RMSEs of the microphysical variables of Zh\_obs\_IM in the later cycles are therefore higher than those of Vr\_obs\_IM, except for  $q_s$ , where  $V_r$  alone is very poor in estimating  $q_s$  (Figure 10(e)–(o)).

Experiment Vr\_obs\_IM (dotted line in Figure 10) produced much better analyses than did Zh\_obs\_IM in

general. In the early cycles,  $V_r$  is more beneficial than  $Z_H$  to  $u$  and  $v$ , while  $Z_H$  is more helpful than  $V_r$  to most microphysical variables except  $q_v$ ,  $q_h$  and  $N_{ti}$ . Although the error reduction rates of  $q_c$ ,  $q_r$ ,  $q_i$ ,  $N_{tc}$ ,  $N_{tr}$ ,  $N_{ts}$  and  $N_{th}$  in the early cycles of Vr\_obs\_IM are slower than those of Zh\_obs\_IM, error increase in the later cycles is weak or absent in these variables. Considering the fact that the wind variables are not directly affected by the PSD-related observation operator error, the better performance with  $V_r$  data compared to  $Z_H$  is reasonable.

When  $Z_H$  is assimilated in addition to  $V_r$ , its positive impact on  $\theta'$ ,  $q_r$ ,  $q_i$ ,  $q_s$ ,  $q_h$ ,  $N_{tr}$ ,  $N_{ti}$ ,  $N_{ts}$  and  $N_{th}$  (Figure 10(d), (g)–(j), (l)–(o)) is clear. Because of the model error, the overall RMSEs of state variables in VrZh\_obs\_IM (thin solid black) are larger than those in EXP-VrZh (thick dotted grey). A larger deterioration of state estimation is found in  $w$ ,  $q_h$ ,  $N_{tr}$ ,  $N_{th}$  and  $q_r$ , with errors that are 150% to 500% larger. This result suggests that the model microphysical processes are more sensitive to the PSDs of rain and hail than to the PSDs of cloud water, ice, and snow. To see if perturbing  $\alpha$  helps improve the results given the use of different microphysics schemes, experiment VrZh\_ptr $\alpha$ \_obs\_IM is performed, which is the same as VrZh\_obs\_IM except that  $\alpha_r$  values ranging from  $-1$  to  $3$  and  $\alpha_h$  values ranging from  $4$  to  $0$  at a constant interval of  $0.05$  are specified for the ensemble members. The use of such perturbed values is found to help reduce the analysis error (thin solid grey in Figure 10) except for  $q_i$ , although the improvement is relatively small.

At 40 min or after four analysis cycles, the basic pattern of reflectivity and surface cold pool structure of VrZh\_obs\_IM is estimated reasonably well, but the intensities of reflectivity and cold pool are weaker than those of truth (Figure 11(a) and (e)). The low-level winds are not well analysed by this time; there exist too-strong southerly flows north of the main storm. Significant microphysics errors must be at least partially responsible while the lack of direct  $V_r$  data there makes it difficult to correct wind error quickly. During the later cycles, such wind errors are gradually corrected, and by 100 min the general wind pattern becomes close to the truth, with the southerly flow bias essentially gone.

## 5. Summary and conclusions

In this study, the ability of an ensemble Kalman filter (EnKF) in estimating two moments (mixing ratios and total number concentrations) of the microphysics particle size distributions (PSDs) for various species as well as all other state variables describing a supercell storm is examined through observing system simulation experiments (OSSEs). Three general scenarios are examined. The first scenario assumes a perfect prediction model and perfect observation operators; the same two-moment (DM) microphysics scheme is used in the truth simulation and in the data assimilation and the same exponential PSD is assumed in both also. The second scenario introduces error in the shape parameter of the gamma PSD within the prediction model while the observation operators remain perfect. In these cases, the reflectivity observation operator of JZX08 is used. In the third scenario, the truth is simulated using a three-moment (TM) microphysics scheme and the reflectivity calculation employs a T-matrix method when simulating the data while the data assimilation uses a DM scheme in the prediction model and the observation operator of JZX08.

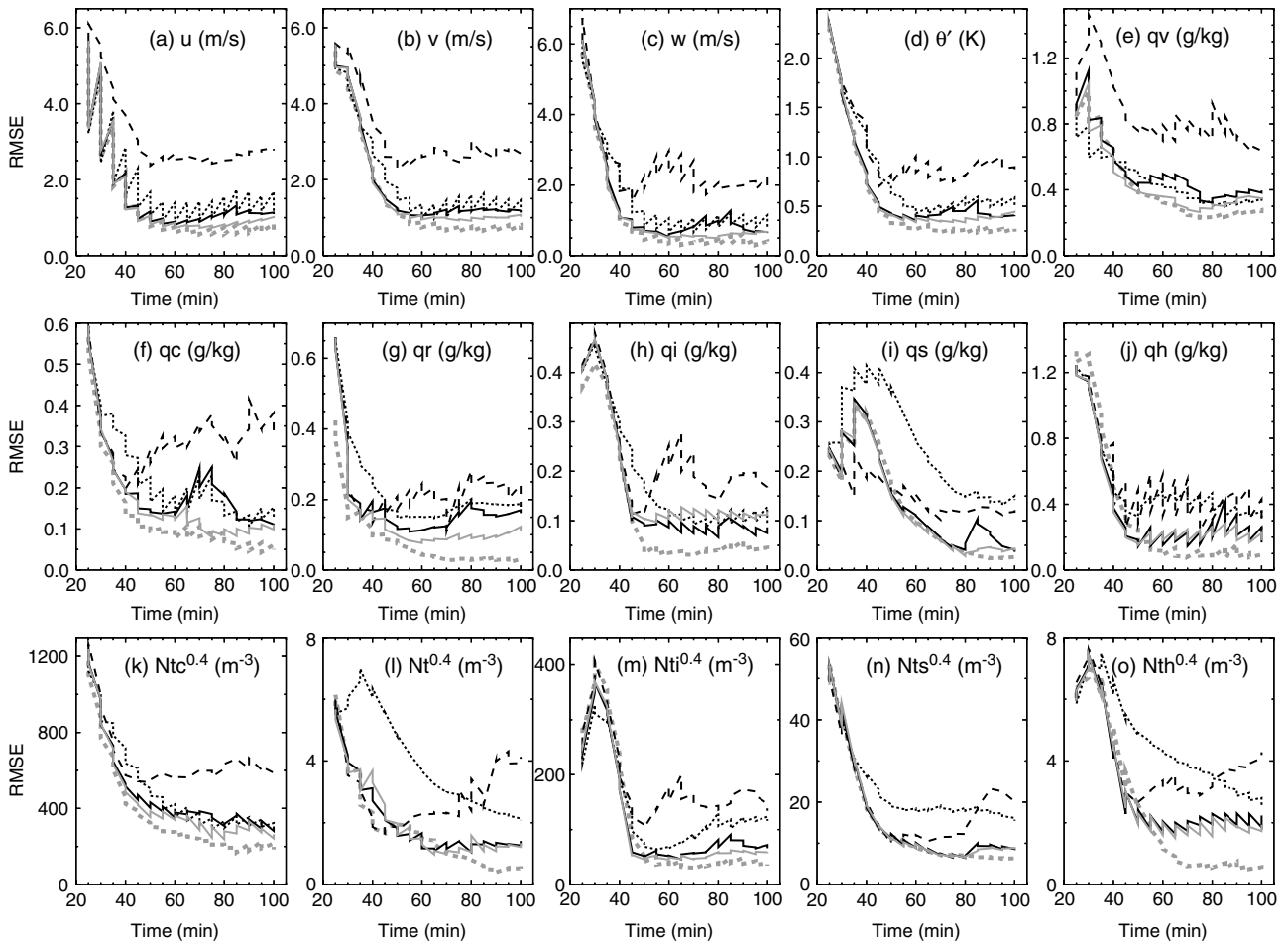


**Figure 10.** As in Figure 2, but for experiments VrZh\_obs\_IM (solid black), Vr\_obs\_IM (dotted black), Zh\_obs\_IM (dashed black), and VrZh\_ptr $\alpha$ \_obs\_IM (thin solid grey). The RMSEs are computed with respect to the truth simulation using the MY three-moment microphysics scheme. The RMSEs of EXP-VrZh (thick dotted grey) are shown for comparison.

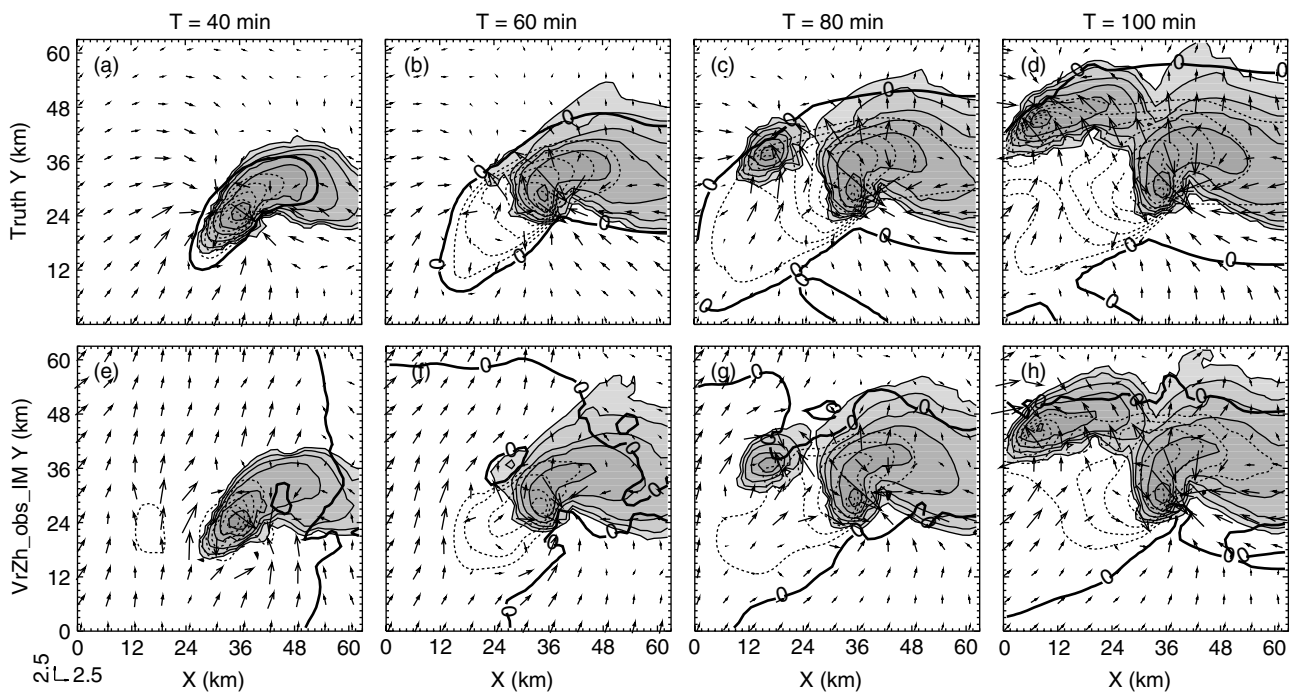


**Figure 11.** As in Figure 1, but for the truth simulation using the TM scheme of MY (a)–(d), and the analyses of experiment VrZh\_obs\_IM (e)–(h). The reflectivity is computed using the radar simulator of JXZ10b.

Significant model errors associated with the PSD shape and microphysics scheme, and with the scattering calculation in the observation operator, are present in this case. The individual and combined impacts of radial velocity ( $V_r$ ) and reflectivity ( $Z_H$ ) data are examined for these three scenarios.

In a perfect-model scenario, when both  $V_r$  and  $Z_H$  data are assimilated, the EnKF system employing a DM scheme is able to accurately estimate the increased number of state variables. Error levels close to those of single-moment (SM) cases are obtained. This finding is significant given the much larger degrees of freedom in the estimation system when a DM scheme is used.

However, when only reflectivity is assimilated, a significant deterioration in the state estimation is found. The non-unique link between state variables and observed reflectivity is believed to be at least part of the cause. The reflectivity corresponding to a hydrometeor category is dependent on its mixing ratio  $q$  and total number concentration  $N_t$ , two independently predicted state variables. A good fit of the analysed reflectivity to the observation does not guarantee good analyses of  $q$  and  $N_t$ . Due to the complex nonlinear microphysical processes involved, the prediction model does not seem to be providing sufficient constraint through the ensemble system. The addition of  $V_r$  data, whose observation operator is not directly affected by microphysics, is very helpful; the  $V_r$  data provide additional constraints to reduce the error in the final solution.

The forecast error correlations between model state variables and simulated reflectivity in the updraught core show differences between the SM and DM cases. Positive correlation is found in the SM case in an earlier study while negative correlation is found in our current DM case. A hypothesis for this negative correlation is proposed; but its actual validation would require further study.

The EnKF performance in the presence of forecast model error and/or observation operator error is also investigated. The results show that model error can cause noticeable deterioration in the estimation of microphysical state variables when the prediction model is subject to the microphysical parametrization error related to assumed PSD shape and/or to radar scattering calculation. Nevertheless, the estimated dynamic, thermodynamic and microphysical fields are still reasonable even in the presence of such errors, especially when both  $Z_H$  and  $V_r$  data are assimilated. Not affected by the PSD error,  $V_r$  data are able to produce relatively accurate wind analyses with or without  $Z_H$  data. However,  $Z_H$  data are necessary to suppress spurious cells in the otherwise echo-free regions. When the shape parameter  $\alpha$  of a gamma PSD is uncertain, using perturbed values within a reasonable range in the ensemble is found to alleviate the impact of parameter error, resulting in much better estimates of the relevant state variables than using a single incorrect value.

In real scenarios, we may encounter model errors arising from different sources, such as insufficient spatial resolution and misrepresentation of other physical processes. These model errors can dominate the error growth during the assimilation cycles and lead to filter divergence (Houtekamer *et al.*, 2005). To account for model error in ensemble data assimilation systems, various methods have been proposed, such as performing simultaneous parameter estimation. However, using more-accurate parametrization schemes is a more direct, better solution. The use of multi-moment

microphysics schemes is a step towards this direction, while, at the same time, the need to initialize more model state variables poses additional challenges. The latter is the focus of this paper. It is our plan to apply this system to real-data cases in the near future.

## Acknowledgements

The authors thank Daniel Dawson for valuable discussions on the two-moment microphysics scheme. This work was primarily supported by NSF grants EEC-0313747 and ATM-0608168. Ming Xue was also supported by NSF grants ATM-0530814, ATM-0750790, ATM-0802888, ATM-0941491 and OCI-0905040, and by grant No. 40620120437 from the Chinese Natural Science Foundation. Computations were performed at the Oklahoma Supercomputing Center for Education and Research.

## References

- Anderson JL. 2001. An ensemble adjustment Kalman filter for data assimilation. *Mon. Weather Rev.* **129**: 2884–2903.
- Brandes EA, Zhang G, Vivekanandan J. 2002. Experiments in rainfall estimation with a polarimetric radar in a subtropical environment. *J. Appl. Meteorol.* **41**: 674–685.
- Cifelli R, Williams CR, Rajopadhyaya DK, Avery SK, Gage KS, May PT. 2000. Drop-size distribution characteristics in tropical mesoscale convective systems. *J. Appl. Meteorol.* **39**: 760–777.
- Cooper WA. 1986. Ice initiation in natural clouds. Pp 29–32 in *Precipitation enhancement: A scientific challenge*, Braham RR Jr (ed). *Meteorol. Monogr.* 21: No. 43. Amer. Meteorol. Soc.
- Courtier P, Talagrand O. 1987. Variational assimilation of meteorological observations with the adjoint vorticity equation. II: Numerical results. *Q. J. R. Meteorol. Soc.* **113**: 1329–1347.
- Dawson DT II, Xue M, Milbrandt JA, Yau MK, Zhang G. 2007. 'Impact of multi-moment microphysics and model resolution on predicted cold pool and reflectivity intensity and structures in the Oklahoma tornadic supercell storms of 3 May 1999.' Paper 10B.2 in *22nd Conf. on weather analysis and forecasting/18th on NWP*, Park City, Utah, USA, 25–29 June 2007.
- Dawson DT II, Xue M, Milbrandt JA, Yau MK. 2010. Comparison of evaporation and cold pool development between single-moment and multi-moment bulk microphysics schemes in idealized simulations of tornadic thunderstorms. *Mon. Weather Rev.*, in press, doi:10.1175/2009MWR2956.1.
- Doviak RJ, Zrnić DS. 1993. *Doppler radar and weather observations*. 2nd edition. Academic Press.
- Dowell DC, Zhang F, Wicker LJ, Snyder C, Crook NA. 2004. Wind and temperature retrievals in the 17 May 1981 Arcadia, Oklahoma, supercell: Ensemble Kalman filter experiments. *Mon. Weather Rev.* **132**: 1982–2005.
- Evensen G. 1994. Sequential data assimilation with a nonlinear quasi-geostrophic model using Monte Carlo methods to forecast error statistics. *J. Geophys. Res.* **99**(C5): 10143–10162.
- Ferrier BS. 1994. A double-moment multiple-phase four-class bulk ice scheme. Part I: Description. *J. Atmos. Sci.* **51**: 249–280.
- Ferrier BS, Tao W-K, Simpson J. 1995. A double-moment multiple-phase four-class bulk ice scheme. Part II: Simulations of convective storms in different large-scale environments and comparisons with other bulk parameterizations. *J. Atmos. Sci.* **52**: 1001–1033.
- Gilmore MS, Straka JM, Rasmussen EN. 2004. Precipitation uncertainty due to variations in precipitation particle parameters within a simple microphysics scheme. *Mon. Weather Rev.* **132**: 2610–2627.
- Green AW. 1975. An approximation for the shapes of large raindrops. *J. Appl. Meteorol.* **14**: 1578–1583.
- Hogan RJ. 2007. A variational scheme for retrieving rainfall rate and hail reflectivity fraction from polarimetric radar. *J. Appl. Meteorol. Clim.* **46**: 1544–1564.
- Hong S-Y, Lim J-OJ. 2006. The WRF single-moment 6-class microphysics scheme (WSM6). *J. Korean Meteorol. Soc.* **42**: 129–151.
- Houtekamer PL, Mitchell HL. 1998. Data assimilation using an ensemble Kalman filter technique. *Mon. Weather Rev.* **126**: 796–811.
- Houtekamer PL, Mitchell HL, Pellerin G, Buehner M, Charron M, Spack L, Hansen B. 2005. Atmospheric data assimilation with an ensemble Kalman filter: Results with real observations. *Mon. Weather Rev.* **133**: 604–620.

- Houze RA Jr, Hobbs PV, Herzegh PH, Parsons DB. 1979. Size distributions of precipitation particles in frontal clouds. *J. Atmos. Sci.* **36**: 156–162.
- Joss J, Waldvogel A. 1969. Raindrop size distribution and sampling size errors. *J. Atmos. Sci.* **26**: 566–569.
- Jung Y, Zhang G, Xue M. 2008a. Assimilation of simulated polarimetric radar data for a convective storm using the ensemble Kalman filter. Part I: Observation operators for reflectivity and polarimetric variables. *Mon. Weather Rev.* **136**: 2228–2245.
- Jung Y, Xue M, Zhang G, Straka JM. 2008b. Assimilation of simulated polarimetric radar data for a convective storm using the ensemble Kalman filter. Part II: Impact of polarimetric data on storm analysis. *Mon. Weather Rev.* **136**: 2246–2260.
- Jung Y, Xue M, Zhang G. 2010a. Simultaneous estimation of microphysical parameters and atmospheric state using simulated polarimetric radar data and ensemble Kalman filter in the presence of observation operator error. *Mon. Weather Rev.* **138**: 539–562.
- Jung Y, Xue M, Zhang G. 2010b. Simulations of polarimetric radar signatures of a supercell storm using a two-moment bulk microphysics scheme. *J. Appl. Meteorol. Clim.*, **49**: 146–163.
- Koenig LR, Murray FW. 1976. Ice-bearing cumulus cloud evolution: Numerical simulation and general comparison against observations. *J. Appl. Meteorol.* **15**: 747–762.
- Kumjian MR, Ryzhkov AV. 2008. Polarimetric signatures in supercell thunderstorms. *J. Appl. Meteorol. Clim.* **47**: 1940–1961.
- Le Dimet F-X, Talagrand O. 1986. Variational algorithms for analysis and assimilation of meteorological observations: Theoretical aspects. *Tellus* **38A**: 97–110.
- Lin Y-L, Farley RD, Orville HD. 1983. Bulk parameterization of the snow field in a cloud model. *J. Appl. Meteorol.* **22**: 1065–1092.
- Lo KK, Passarelli RE Jr. 1982. The growth of snow in winter storms: An airborne observational study. *J. Atmos. Sci.* **39**: 697–706.
- Lord SJ, Kalnay E, Daley R, Emmitt GD, Atlas R. 1997. 'Using OSSEs in the design of the future generation of integrated observing systems.' Pp 45–47 in *Preprints, 1st Symposium on integrated observation systems*, Long Beach, California, USA. Amer. Meteorol. Soc.
- McCumber M, Tao W-K, Simpson J, Penc R, Soong S-T. 1991. Comparison of ice-phase microphysical parameterization schemes using numerical simulations of tropical convection. *J. Appl. Meteorol.* **30**: 985–1004.
- Marshall JS, Palmer WM. 1948. The distribution of raindrops with size. *J. Meteorol.* **5**: 165–166.
- Meng Z, Zhang F. 2007. Tests of an ensemble Kalman filter for mesoscale and regional-scale data assimilation. Part II: Imperfect model experiments. *Mon. Weather Rev.* **135**: 1403–1423.
- Milbrandt JA, Yau MK. 2005a. A multimoment bulk microphysics parameterization. Part I: Analysis of the role of the spectral shape parameter. *J. Atmos. Sci.* **62**: 3051–3064.
- Milbrandt JA, Yau MK. 2005b. A multimoment bulk microphysics parameterization. Part II: A proposed three-moment closure and scheme description. *J. Atmos. Sci.* **62**: 3065–3081.
- Milbrandt JA, Yau MK. 2006. A multimoment bulk microphysics parameterization. Part IV: Sensitivity experiments. *J. Atmos. Sci.* **63**: 3137–3159.
- Morrison H, Curry JA, Khvorostyanov VI. 2005. A new double-moment microphysics parameterization for application in cloud and climate models. Part I: Description. *J. Atmos. Sci.* **62**: 1665–1677.
- Ray PS, Johnson BC, Johnson KW, Bradberry JS, Stephens JJ, Wagner KK, Wilhelmson RB, Klemp JB. 1981. The morphology of severe tornadic storms on 20 May 1977. *J. Atmos. Sci.* **38**: 1643–1663.
- Rogers RR, Yau MK. 1989. *A short course in cloud physics*. 3rd edition. Pergamon Press.
- Snook N, Xue M. 2008. Effects of microphysical drop size distribution on tornadogenesis in supercell thunderstorms. *Geophys. Res. Lett.* **35**: L24803, doi:10.1029/2008GL035866.
- Snyder C, Zhang F. 2003. Assimilation of simulated Doppler radar observations with an ensemble Kalman filter. *Mon. Weather Rev.* **131**: 1663–1677.
- Talagrand O, Courtier P. 1987. Variational assimilation of meteorological observations with the adjoint vorticity equation. I: Theory. *Q. J. R. Meteorol. Soc.* **113**: 1311–1328.
- Tong M, Xue M. 2005. Ensemble Kalman filter assimilation of Doppler radar data with a compressible nonhydrostatic model: OSS experiments. *Mon. Weather Rev.* **133**: 1789–1807.
- Tong M, Xue M. 2008a. Simultaneous estimation of microphysical parameters and atmospheric state with simulated radar data and ensemble square root Kalman filter. Part I: Sensitivity analysis and parameter identifiability. *Mon. Weather Rev.* **136**: 1630–1648.
- Tong M, Xue M. 2008b. Simultaneous estimation of microphysical parameters and atmospheric state with simulated radar data and ensemble square root Kalman filter. Part II: Parameter estimation experiments. *Mon. Weather Rev.* **136**: 1649–1668.
- Ulbrich CW. 1983. Natural variations in the analytical form of the raindrop size distribution. *J. Appl. Meteorol.* **22**: 1764–1775.
- van den Heever SC, Cotton WR. 2004. The impact of hail size on simulated supercell storms. *J. Atmos. Sci.* **61**: 1596–1609.
- Vivekanandan J, Adams WM, Bringi VN. 1991. Rigorous approach to polarimetric radar modeling of hydrometeor orientation distributions. *J. Appl. Meteorol.* **30**: 1053–1063.
- Waterman PC. 1969. Scattering by dielectric obstacles. *Alta Freq. (Speciale)* **38**: 348–352.
- Whitaker JS, Hamill TM. 2002. Ensemble data assimilation without perturbed observations. *Mon. Weather Rev.* **130**: 1913–1924.
- Xue M, Droegemeier KK, Wong V. 2000. The Advanced Regional Prediction System (ARPS) – A multiscale nonhydrostatic atmospheric simulation and prediction tool. Part I: Model dynamics and verification. *Meteorol. Atmos. Phys.* **75**: 161–193.
- Xue M, Droegemeier KK, Wong V, Shapiro A, Brewster K, Carr F, Weber D, Liu Y, Wang D-H. 2001. The Advanced Regional Prediction System (ARPS) – A multiscale nonhydrostatic atmospheric simulation and prediction tool. Part II: Model physics and applications. *Meteorol. Atmos. Phys.* **76**: 143–165.
- Xue M, Wang D, Gao J, Brewster K, Droegemeier KK. 2003. The Advanced Regional Prediction System (ARPS), storm-scale numerical weather prediction and data assimilation. *Meteorol. Atmos. Phys.* **82**: 139–170.
- Xue M, Tong M, Droegemeier KK. 2006. An OSSE framework based on the ensemble square root Kalman filter for evaluating the impact of data from radar networks on thunderstorm analysis and forecasting. *J. Atmos. Oceanic Technol.* **23**: 46–66.
- Xue M, Jung Y, Zhang G. 2007. Error modeling of simulated reflectivity observations for ensemble Kalman filter assimilation of convective storms. *Geophys. Res. Lett.* **34**: L10802, doi:10.1029/2007GL029945.
- Zhu Y, Navon IM. 1999. Impact of parameter estimation on the performance of the FSU global spectral model using its full-physics adjoint. *Mon. Weather Rev.* **127**: 1497–1517.